

# There and Back Again: On the relation between Noise and Image Inversions in Diffusion Models

Łukasz Staniszewski<sup>1\*</sup>

Łukasz Kuciński<sup>2,3,4</sup>

Kamil Deja<sup>1,4</sup>

<sup>1</sup>Warsaw University of Technology

<sup>2</sup>University of Warsaw

<sup>3</sup>Polish Academy of Sciences

<sup>4</sup>IDEAS NCBR

## Abstract

Diffusion Models achieve state-of-the-art performance in generating new samples but lack low-dimensional latent space that encodes the data into meaningful features. Inversion-based techniques try to solve this issue by reversing the denoising process and mapping images back to their approximated starting noise. In this work, we thoroughly analyze this procedure and focus on the relation between the initial Gaussian noise, the generated samples, and their corresponding latent encodings obtained through the DDIM inversion. First, we show that latents exhibit structural patterns in the form of less diverse noise predicted for smooth image regions. Next, we explain the origin of this phenomenon, demonstrating that, during the first inversion steps, the noise prediction error is much more significant for the plain areas than for the rest of the image. Finally, we present the consequences of the divergence between latents and noises by showing that the space of image inversions is notably less manipulative than the original Gaussian noise. This leads to a low diversity of generated interpolations or editions based on the DDIM inversion procedure and ill-defined latent-to-image mapping. Code is available at <https://github.com/luk-st/ta>.

## 1. Introduction

Diffusion-based probabilistic models (DMs) [43], have achieved state-of-the-art results in many generative domains including image [7], speech [37], video [15], and music [28] synthesis. Nevertheless, one of the significant drawbacks that distinguish diffusion-based approaches from other generative models like Variational Autoencoders (VAEs) [23] is the lack of implicit latent space that encodes the images into low-dimensional, interpretable, or editable representations. To mitigate this issue, several works seek meaningful relations in the starting noise used for generations. This method, known as an inversion technique, was introduced with De-

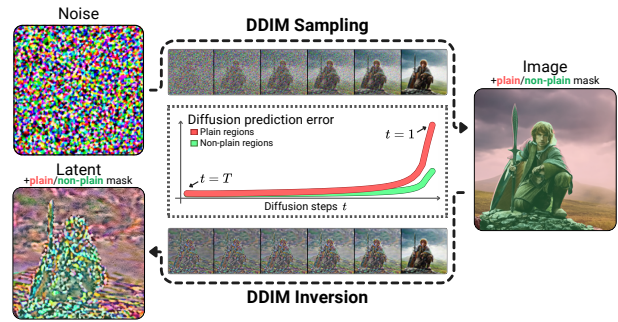


Figure 1. **DDIM inversion produces latent encodings that exhibit less diverse noise in the smooth image areas than in the non-plain one.** Through in-depth analysis, we attribute this problem to the errors of noise prediction in the first inversion steps.

noising Diffusion Implicit Models (DDIM) [44], but led to the proliferation of works [10, 16, 17, 29, 32, 35]. The core idea is to use a denoising diffusion model to predict noise and add it to the image instead of subtracting it. Repeating this process multiple times effectively traces the backward diffusion trajectory, approximating the original *noise* that could have generated the *image*. However, due to approximation errors and biases introduced by the trained denoising model, discrepancies arise between the initial Gaussian noise and the reconstructed *latent* representation.

While recent works [10, 17, 32, 35, 58] try to improve the inversion procedure from the perspective of tasks such as image reconstruction, editing or interpolation, in this work, we propose to focus solely on the inversion mechanism itself and closely study the errors that DDIM inversion introduces.

To that end, we analyze the relation between sampled Gaussian noise, generated images, and their inverted latent encodings. First, we review existing studies and conduct additional analyses demonstrating that the reverse DDIM technique produces latent representations with pixel correlations that deviate significantly from a Normal distribution. We then experimentally show that this deviation manifests as lower diversity in latent codes, particularly in regions cor-

\*Corresponding author: [luks.staniszewski@gmail.com](mailto:luks.staniszewski@gmail.com)

responding to smooth image surfaces. To further investigate the cause of this phenomenon, we find that the approximation error of DDIM inversion is higher for pixels representing smooth areas than for other parts of the image. Additionally, we show that this error discrepancy occurs predominantly during the initial steps of the inversion process.

To present the consequences of the observed divergence, we analyze the effects of using latent embeddings instead of raw noise in practical DM applications. Our results show that the latent space is less adaptable for manipulation compared to the noise space. This limitation is particularly noticeable in lower-quality interpolations between randomly chosen latents and less expressive edits, especially in smooth regions of source images. In our final experiment, we revisit the previous observation to highlight that this issue primarily arises during the early stages of the image inversion process, as replacing just 6% of initial steps with ground truth values from the backward diffusion pass significantly mitigates observed limitations.

Our main contributions can be summarized as follows:

- We show that reverse DDIM produces latent representations that deviate from Normal distribution mostly because of less diverse values for the parts of the latents corresponding to the plain image surfaces.
- We explain the origins of this phenomenon, showing that the inversion approximation error is more notable for the plain pixel areas, especially during the first noising steps.
- We show that as a consequence of this divergence, the resulting latent space is less manipulative, which leads to the lower quality of interpolations and edits generated from latent variables as a starting state.

## 2. Background and Related Work

**Denoising Diffusion Implicit Models.** The training of DMs consists of forward and backward diffusion processes, where in the context of Denoising Diffusion Probabilistic Models (DDPMs [14]), the former one with training image  $x_0$  and a variance schedule  $\{\beta_t\}_{t=1}^T$ , can be expressed as

$$x_t = \sqrt{\bar{\alpha}_t}x_0 + \sqrt{1 - \bar{\alpha}_t}\epsilon_t, \quad (1)$$

with  $\alpha_t = 1 - \beta_t$ ,  $\bar{\alpha}_t = \prod_{s=1}^t \alpha_s$ , and  $\epsilon_t \sim \mathcal{N}(0, \mathcal{I})$ .

In the backward process, the noise is gradually removed starting from a random noise  $x_T \sim \mathcal{N}(0, \mathcal{I})$  for  $t = T \dots 1$ , with intermediate steps defined as:

$$x_{t-1} = \underbrace{\sqrt{\bar{\alpha}_{t-1}} \cdot (x_t - \sqrt{1 - \bar{\alpha}_t} \cdot \epsilon_\theta^{(t)}(x_t, c)) / \sqrt{\bar{\alpha}_t}}_{x_0 \text{ prediction}} + \underbrace{\sqrt{1 - \bar{\alpha}_{t-1} - \sigma_t^2} \cdot \epsilon_\theta^{(t)}(x_t, c) + \sigma_t z_t}_{\text{direction pointing to } x_t}, \quad (2)$$

where  $\epsilon_\theta^{(t)}(x_t, c)$  is an output of a neural network (such as U-Net), and can be expressed as a combination of clean

image ( $x_0$ ) prediction, a direction pointing to previous denoising step ( $x_t$ ), and a stochastic factor  $\sigma_t z_t$ , where  $\sigma_t = \eta \sqrt{\beta_t(1 - \bar{\alpha}_{t-1}) / (1 - \bar{\alpha}_t)}$  and  $z_t \sim \mathcal{N}(0, \mathcal{I})$ .

In the standard DDPM model [14], the  $\eta$  parameter is set to  $\eta = 1$ . However, changing it to  $\eta = 0$  makes the whole process a deterministic Denoising Diffusion Implicit Model (DDIM) [44], a class of DMs we target in this work.

One of the advantages of DDIM is that by making the process deterministic, we can encode images back to the noise space. The inversion can be obtained by rewriting Eq. (2) as

$$x_t = \sqrt{\bar{\alpha}_t}x_{t-1} + (\sqrt{1 - \bar{\alpha}_t} - \sqrt{\alpha_t - \bar{\alpha}_t}) \cdot \epsilon_\theta^{(t)}(x_t, c) \quad (3)$$

However, due to circular dependency on  $\epsilon_\theta^{(t)}(x_t, c)$ , Dhariwal and Nichol [7] propose to approximate this equation by assuming the local linearity between directions  $x_{t-1}$  to  $x_t$  and  $x_t$  to  $x_{t+1}$ , which implies that the model’s prediction in  $t$ -th inversion step can be approximated using  $x_{t-1}$  as an input, *i.e.*,

$$\epsilon_\theta^{(t)}(x_t, c) \approx \epsilon_\theta^{(t)}(x_{t-1}, c). \quad (4)$$

While such approximation is often sufficient to obtain good reconstructions of images, it introduces the error dependent on the difference ( $x_t - x_{t-1}$ ), which can be detrimental for models that sample images with a few diffusion steps or use the classifier-free guidance [13, 32] for better prompt adherence. As a result, also noticed by recent works [10, 35], latents resulting from DDIM inversion do not follow the definition of Gaussian noise because of the existing pixel correlations. In this work, we empirically study this phenomenon and explain its origin. We discuss the relations between the following three variables:

- **Gaussian noise variable**,  $\mathbf{x}_T$ , used as an input to generate an image through a backward diffusion process.
- **Image sample**,  $\mathbf{x}_0$ , the outcome of the generation process produced by the Diffusion Model.
- **Latent encoding**,  $\hat{\mathbf{x}}_T$ , the result of the DDIM inversion procedure as introduced in Eq. (3).

**Image-to-noise inversion techniques.** The DDIM inversion, despite the noise approximation errors, forms the foundation for many applications, including inpainting [53], interpolation [7, 58], and edition [3, 6, 12, 21, 47].

Several works [2, 4, 8, 10, 11, 16–18, 27, 29, 31, 32, 34, 35, 48–50, 57] aim to reverse the denoising process in text-to-image models, where prompt embeddings can strongly affect the final latent representation through Classifier-free guidance (CFG) [13]. Null-text inversion [32] extends the DDIM inversion with additional null-embedding optimization, reducing the image reconstruction error. Other techniques, improve inversion for image editing through seeking embeddings [8, 11, 31] or leveraging DDIM latents [4] for guidance. On the other hand, some works leverage additional numerical methods [10, 16, 29, 34] to minimize inversion

error. In particular, Renoise [10] iteratively improves the prediction of added noise in each diffusion step via predictor-corrector technique. Huberman-Spiegelglas et al. [17] followed by Brack et al. [2] propose inversion methods for non-probabilistic diffusion models (DPMs), enabling the creation of various image edition results via inversion. Finally, to reduce the discrepancy between DDIM latents and Gaussian noises, Parmar et al. [35] propose to additionally regularize final DDIM Inversion outputs for better image editing, while Lin et al. [27] introduce alternative noise scheduler to improve inversion stability.

**Noise-to-image mapping in diffusion models.** While in this work, we focus mostly on the differences between random noise, associated generations, and their inversions, several works investigate interesting properties between the initial random noise and generations that result from the training objective of DDPMs and score-based models. Kadkhodaie et al. [19] show that due to inductive biases of denoising models, different DDPMs trained on similar datasets converge to almost identical solutions. This idea is further explored by Zhang et al. [54], observing that even models with different architectures converge to the same score function and, hence, the same noise-to-generations mapping. Khrulkov and Oseledets [20] show that diffusion models’ encoder map coincides with the optimal transport (OT) map when modeling simple distributions. However, other works [22, 25] contradict this result. In this work, we extend the analysis further by cross-checking mappings between images with their noises or latents created with DDIM inversion.

### 3. Experiments

In this section, we provide a series of empirical observations on the relation between sampled noises, their generations, and latent representations.

#### 3.1. Experimental details

We employ diffusion models working directly in the pixel space or in the latent space of the autoencoder. In the case of the former ones, we use UNet-based architectures, including three unconditional Ablated Diffusion Models (ADMs, [7]) in three different image resolution settings:  $32 \times 32$ ,  $64 \times 64$ , and  $256 \times 256$ , and Deepfloyd IF [46], text-to-image generative model sampling images in  $64 \times 64$  resolution. Additionally, we explore the unconditional Latent Diffusion Model (LDM, [39]) with a U-Net model as a backbone and class-conditional Diffusion Transformer (DiT, [36]), which performs diffusion process in the latent space as well. Studied models were trained on diverse datasets, including CIFAR-10, ImageNet, CelebA-HQ, and LAION-A, as presented in Tab. 1. We use original trained checkpoints provided by the authors of those works. Both DiT and IF are conditional models that employ CFG for better prompt adherence.

Property	ADM-32	ADM-64	ADM-256	LDM	DiT	IF
Diffusion	Pixel	Pixel	Pixel	Latent	Latent	Pixel
Image res.	$32 \times 32$	$64 \times 64$	$256 \times 256$	$256 \times 256$	$256 \times 256$	$64 \times 64$
Latent res.	-	-	-	$3 \times 64 \times 64$	$4 \times 32 \times 32$	-
Trainset	CIFAR-10	ImageNet	ImageNet	CelebA	ImageNet	LAION-A
Cond?	✗	✗	✗	✗	✓	✓
Backbone	U-Net	U-Net	U-Net	U-Net	DiT	U-Net

Table 1. **Overview of diffusion models used for our experiments.** We study both unconditioned and conditioned models, operating in both pixel and latent spaces.

For conditioning, we provide prompts from Recap-COCO-30K dataset [26] for IF and ImageNet class names for DiT. However, as noted by Mokady et al. [32], cfg introduces additional error to the DDIM inversion, so to focus solely on the inversion approximation error in our setup, we disable cfg by setting the guidance scale to  $w = 1$ .

For sampling, we use the DDIM sampler and, unless stated otherwise, set  $T = 100$  diffusion steps for both sampling and inverting to the latent encodings.

#### 3.2. Latents vs. noise

Reversed sampling (inversion) process provides the foundation for methods created for diverse applications. The underlying assumption of those methods is that by encoding the *image* back with a denoising model, we can obtain the original *noise* that can be used to reconstruct or manipulate the image. In this work, we challenge this assumption and ask the first question:

**Research Question 1:** Are there any differences between sampled Gaussian noise and latents calculated through the DDIM inversion?

**Prior work and findings.** Several recent works highlight that outputs of the DDIM inversion differ from the standard Gaussian noise [10, 35] and that the difference can be attributed to the approximation error [16, 27, 49]. In particular, Parmar et al. [35], followed by Garibi et al. [10], observe that latents “do not follow the statistical properties of uncorrelated, Gaussian white noise, causing poor editability”.

**Experiments.** First, we confirm existing claims on the presence of correlations in the latent encodings ( $\hat{x}_T$ ) by comparing them to images ( $x_0$ ) and noises ( $x_T$ ) across diverse diffusion architectures. In Tab. 2, we calculate a mean of top-20 Pearson correlation coefficients (their absolute values) inside  $C \times 8 \times 8$  pixel patches, where  $C$  is a number of channels (pixel RGB colors or latent space dimensions for latent models). The results, calculated with 10000 samples, confirm that latent representations have significantly more correlated pixels than the independent Gaussian noises.

In Fig. 2, we show how the measured correlations manifest themselves in the latent codes calculated with inverse DDIM. For pixel models such as Deepfloyd IF, we observe

Model	Noise ( $\mathbf{x}_T$ )	Latent ( $\hat{\mathbf{x}}_T$ )	Sample ( $\mathbf{x}_0$ )
ADM-32	0.039 $\pm$ .003	0.382 $\pm$ .010	0.964 $\pm$ .022
ADM-64	0.039 $\pm$ .003	0.126 $\pm$ .008	0.925 $\pm$ .021
ADM-256	0.039 $\pm$ .003	0.161 $\pm$ .013	0.960 $\pm$ .008
IF	0.039 $\pm$ .003	0.498 $\pm$ .025	0.936 $\pm$ .019
LDM	0.039 $\pm$ .003	0.045 $\pm$ .014	0.645 $\pm$ .099
DiT	0.041 $\pm$ .003	0.103 $\pm$ .021	0.748 $\pm$ .064

Table 2. Mean of top-20 Pearson correlation coefficients inside  $8 \times 8$  patches for random Gaussian noises, latent encodings, and generated samples. Latents created with the reverse DDIM procedure are much more correlated than noises.

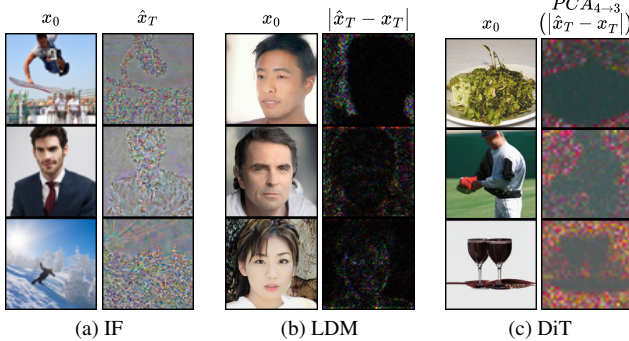


Figure 2. **Latent encodings exhibit image patterns.** For small pixel-space models (a), we can observe correlations directly in the inversion results. For bigger models, especially LDMs, the same patterns can be observed in the absolute errors between the latents and the noise (b). This observation also holds for LDM models operating on 4-channels, where we use PCA for visualization (c).

clear groups of correlated pixels as presented in Fig. 2a. For more complex diffusion architectures, such as latent diffusion models, we can highlight the inversion error by plotting the difference between the latent and the noise, as presented in Fig. 2b. This property holds also for LDMs with a 4-channel latent space, where Principal Component Analysis (PCA) is used to present the differences between the latents and noise for the DiT model (Fig. 2c).

**Conclusion.** Our initial experiments in line with related works, demonstrate that latent representations computed using the DDIM inversion deviate from the expected characteristics of independent Gaussian noise. Specifically, both visual analysis and quantitative evaluations reveal significant correlations between the neighboring pixels.

### 3.3. Location of latent encodings space

In this work, we propose to delve further and empirically analyze the nature of this issue. To that end, we first pose the following question:

**Research Question 2:** Is there a common characteristic of the latent encodings that distinguishes them from Gaussian noise?

Model	$\angle \mathbf{x}_0$	$\angle \mathbf{x}_T$	$\angle \hat{\mathbf{x}}_T$
ADM-32	29	28	123
ADM-64	11	60	109
ADM-256	24	73	83
IF	34	40	106
LDM	2	76	102
DiT	4	66	110

Table 3. Most probable angles next to the Gaussian noise  $\mathbf{x}_T$ , generations  $\mathbf{x}_0$ , and latents  $\hat{\mathbf{x}}_T$  across different diffusion models. We use  $T = 100$  denoising and noising steps.

**Experiments.** To answer it, we first investigate the geometric aspect of how the latent encodings are distributed in relation to the original noise and generated samples. We focus on understanding their spatial relationships across different model architectures and configurations.

First, in Tab. 3, we determine the most probable angles formed by noises  $\mathbf{x}_T$ , samples  $\mathbf{x}_0$ , and latents  $\hat{\mathbf{x}}_T$  for each model by binning the empirically observed angles and selecting those that satisfy triangle angle sum, while maximizing the joint probability. We provide details on this methodology and visualization in Appendix B. Results of the experiment show that the angle located at the image and noise vertices (accordingly  $\angle \mathbf{x}_0$  and  $\angle \mathbf{x}_T$ ) are always acute and, in almost every case, the angle by the latent vertex ( $\angle \hat{\mathbf{x}}_T$ ) is obtuse. This property implies that, due to approximation errors in the reverse DDIM process, latents reside in proximity to, but with a measurable offset, from the shortest-path trajectory between the noise distribution and the generated image.

However, the trajectory defined by the backward diffusion process does not necessarily follow the linear path, as DMs learn a score function that is highly non-linear, causing the denoising path to follow the curved structure of the data manifold [45]. Therefore, to further strengthen our analysis, we investigate the location of the latent with respect to the generation trajectory. To that end, we analyze the distance between the next steps  $\{x_t\}_{t=T \dots 1}$  of the backward diffusion process and intermediate points on the linear interpolation path between the noise and the appropriate latent – along the  $\mathbf{x}_T \hat{\mathbf{x}}_T$  side of the noise-sample-latent triangle. We present the results of this experiment in Fig. 3, where each pixel, with coordinates  $(t, \lambda)$ , is colored according to the  $l_2$  distance between the intermediate trajectory step  $x_t$  and the corresponding interpolation step. This distance can be expressed as  $\|(1 - \lambda)\mathbf{x}_T + \lambda\hat{\mathbf{x}}_T - x_t\|_2$ .

We observe that, while moving from the random Gaussian noise ( $\mathbf{x}_T$ ) towards the final sample ( $\mathbf{x}_0$ ), the intermediate steps  $x_t$  approach the latent ( $\hat{\mathbf{x}}_T$ ), while after the transition point present around 50-70% of the generative trajectory the distance to the latent becomes lower than the distance to the starting noise. This observation reveals, that latent encodings retain some characteristics of the original input samples and contain information about the source generation.

To more closely localize the latent encodings, we propose

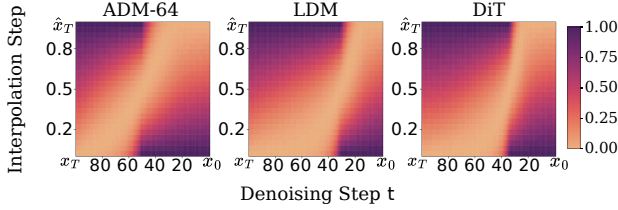


Figure 3.  $l_2$ -distances between intermediate diffusion denoising steps  $x_t$  and points on the linear interpolation path from noise  $x_T$  to the inverted latents  $\hat{x}_T$ . The consecutive intermediate generation steps along the sampling trajectory consequently get closer to the latent variables.

ADM-32	ADM-64	ADM-256	IF	LDM	DiT	Noise
$0.18 \pm 0.33$	$0.71 \pm 1.05$	$0.82 \pm 1.27$	$0.29 \pm 0.53$	$0.98 \pm 1.40$	$0.89 \pm 1.29$	1.00

Table 4. **Variance of the latent encodings ( $\hat{x}_T$ ) calculated with different models.** In comparison, by definition, the variance of initial Gaussian noise equals 1.0.

to study their relations to the center of the analyzed space - point 0 being the mean of the initial noise  $x_T$ . In Tab. 4, we show the average variance of the latent encodings for randomly sampled and inverted 10,000 images. Latent encodings  $\hat{x}_T$  have, in general, lower variance than the noise, which means that the inversion process drives them towards the mean of the Gaussian distribution. The remaining question is how does it manifest?

The visualizations shown in Fig. 2 indicate that, in some cases, we can distinguish the structure of the original objects in the latent encodings. In particular, while the pixels associated with the objects have high diversity, which is also expected for white Gaussian noise, the areas related to the background are much smoother.

This leads to the hypothesis that the most significant difference between the initial Gaussian noises and latent encodings is the limited variance in the areas corresponding to the background of the generated image. To validate it, we compare the properties of resulting latents between plain and non-plain areas in the image. We determine binary masks  $\mathcal{M}_p$  that select smooth surfaces in the image, according to the neighbor differences as described in Appendix C. In Tab. 5, we show that the error between the starting noise  $x_T$  and the latent  $\hat{x}_T$  resulting from the DDIM inversion is higher for pixels corresponding to the plain areas. Across all the models, this trend goes along with a decrease in the standard deviation of latents’ pixels related to those image regions. It suggests that DDIM inversion struggles with reversing the denoising operation for those image parts, bringing them to 0 (average) and reducing their diversity.

**Conclusion.** Latent encodings resulting from the DDIM Inversion deviate from the Gaussian noises towards zero values. This can be attributed to the less diverse values for parts of the latents corresponding to the plain image surfaces.

Model	Mean Absolute Error		Standard Deviation	
	Plain	Non-plain	Plain	Non-plain
ADM-32	0.49	0.43	0.34	0.46
ADM-64	0.22	0.15	0.49	0.64
ADM-256	0.39	0.29	0.53	0.66
IF	0.56	0.40	0.46	0.72
LDM	0.13	0.03	0.45	0.59
DiT	0.12	0.06	0.43	0.54

Table 5. **Average per-pixel absolute error (between noise and latent encodings) and standard deviation of the latents’ pixels corresponding to the plain and non-plain areas in images.** The error for plain pixels, where latents are less diverse, is higher than for other regions.

### 3.4. Origin of the divergence

Given the observation from the previous section, we now investigate the possible source of the differences between latents and their corresponding noises, posing the question:

**Research Question 3:** What is the reason behind the specific divergence between input noise and latent calculated with DDIM inversion?

**Experiments.** We first recall that the DDIM Inversion error can be attributed to the approximation of the diffusion model’s output at step  $t \in 1 \dots T$  with the output from step  $t - 1$  (see Eq. (4)). Hence, we can define the inversion approximation error for step  $t$  as the difference between DMs output for the target and previous timesteps  $t$  and  $t - 1$  as:

$$\xi(t) = \underbrace{|\epsilon_\theta^{(t)}(x_t, c)|}_{\mathcal{E}_t^I} - \underbrace{|\epsilon_\theta^{(t)}(x_{t-1}, c)|}_{\mathcal{E}_t^S}, \quad (5)$$

where  $\mathcal{E}_t^S$  is the ground truth DM output for inversion step while  $\mathcal{E}_t^I$  is the approximated prediction.

Based on the observations from the previous section, we propose to investigate how the inversion approximation error  $\xi(t)$  differs for pixels associated with plain and non-plain image areas throughout the following diffusion steps. To that end, we average the approximation errors for 4000 images for each of the  $T = 50$  diffusion timesteps. To ascertain that we measure the error solely for the analyzed step  $t$ , we start the inversion procedure from the ground truth value for step  $(t + 1)$  assuming perfect inversion for each timestep above  $t$ . We split the latent pixels into plain and non-plain areas according to the masks calculated for final generations. We explain this setup in detail in Appendix D.

In Fig. 4, we present the visualization of calculated differences for each diffusion step. As visible, there is a significant difference in the prediction errors for plain and non-plain areas, especially in the initial steps of the noising process. Additionally, in Tab. 6, we show the actual values of the approximation error. By splitting the inversion process into two parts, we can observe that the first 10% of inversion steps

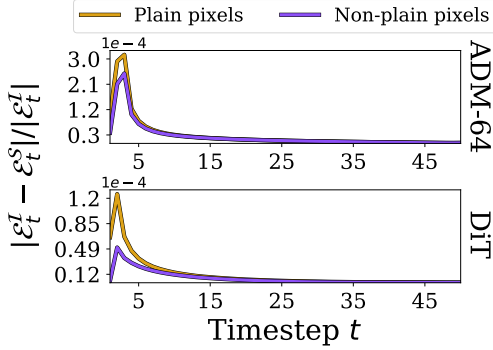


Figure 4. **Inversion approximation error is significantly higher during the first steps of the inversion process than for the next steps.** Moreover, in the first steps, errors for plain areas contribute more significantly to the error than errors for non-plain pixels.

Pixel area	Diffusion steps		Model	
			ADM-64	DiT
Plain	1, 2...50	100%	15.11	5.67
Non-plain			12.43	3.16
Plain	1, 2...5	10%	9.23	3.41
Non-plain			6.80	1.42
Plain	6, 7...50	90%	5.87	2.23
Non-plain			5.63	1.74

Table 6. **Sum of the normalized diffusion model prediction error  $\bar{\mathcal{E}}_{(t_s, t_e)}^E$  during the DDIM inversion for plain and non-plain pixels.** Inversion approximation error is higher for the pixels related to the plain image areas, especially in the first 10% inversion steps that contribute to the error more than the remaining 90% of steps. Values in the table are multiplied by  $10^4$ .

contribute more to the final error than the remaining 90%. Notably, the error in plain areas predominantly accumulates within this first 10% of the inversion steps.

**Conclusion.** Differences between noises and latents can be attributed to the higher approximation error for the pixels related to the plain image areas, especially in the first DDIM inversion steps.

## 4. Consequences of the differences

After identifying the differences between the Gaussian noises and latents and highlighting the origin of the phenomenon, we finally pose the last question:

**Research Question 4:** What are the practical consequences of the divergence between noises and inverse DDIM latents?

Based on the preceding observations, we hypothesize that the less diverse areas in latent variables, connected to smoothed regions in the images, negatively impact their applicability as priors for the generative process. In this section, we showcase several consequences of this problem,

including worse performance in the task of image interpolation and editing, collapsing diversity of generations, and inconsistencies in noise-image mapping.

### 4.1. Interpolation quality

We first adhere to the task of image interpolation, where, for two given images, the goal is to generate a sequence of semantically meaningful intermediary frames between them. Classic techniques based on the pixels’ morphing [52] fail to produce content beyond provided inputs [55], leading to outputs with unnatural artifacts. Therefore, numerous methods [1, 7, 41, 44, 55, 58] leverage diffusion models with noise representations of images in order to obtain realistic transitions between them. Song et al. [44] propose to use the latent variables resulting from the DDIM inversion technique and interpolate them with the spherical linear interpolation (SLERP [42]), that, for two objects  $x$  and  $y$ , is defined as

$$z^{(\lambda)} = \frac{\sin(1-\lambda)\theta}{\sin\theta}x + \frac{\sin\lambda\theta}{\sin\theta}y, \quad (6)$$

where  $\lambda \in [0; 1]$  is an interpolation coefficient and  $\theta = \arccos((x \cdot y) / (\|x\| \|y\|))$ .

We compare the quality of interpolations in the noise space and the latent space. To this end, we sample  $N = 20k$  noises, use DDIM with  $T = 50$  diffusion steps to generate images, and invert those images back into the latents. Next, we randomly assign pairs of either two noises or latents, which we interpolate with SLERP for  $\lambda \in \{0, \frac{1}{6}, \frac{1}{3}, \frac{1}{2}, \frac{2}{3}, \frac{5}{6}, 1\}$  and denoise. In Fig. 5, we show that, by calculating FID-10k to the training set, intermediate noise generations preserve consistent quality along the entire interpolation path. In contrast, this quality collapses for the setting with latents as inputs, especially when both of them contribute equally to the intermediate interpolation point.

In the following rows, we show that worse interpolation results for latents stem from the decline in the variety of produced generations, as indicated by a lower recall [24], especially in the middle of the interpolation path.

### 4.2. Diversity in conditional generation

Text-to-image diffusion models are often combined with deterministic schedulers to manipulate the samples by starting from the same noise and modifying the denoising trajectory with a different prompt. This method, combined with inversion, is widely used to modify real images [10, 12, 17, 32]. However, knowing that DDIM latents are less diverse in plain areas, we hypothesize that using them as a starting state for backward diffusion limits the edited generations.

To evaluate this, we leverage DiT [36] and IF [46] as conditional DMs with  $T = 50$  diffusion steps. For each model, we construct two sets of 1280 randomly selected prompts (ImageNet classes for DiT, COCO-30K [26] prompts for IF): (1) source prompts  $P_S$ , used during the generation and inversion, and (2) target prompts  $P_T$ , used during editing.

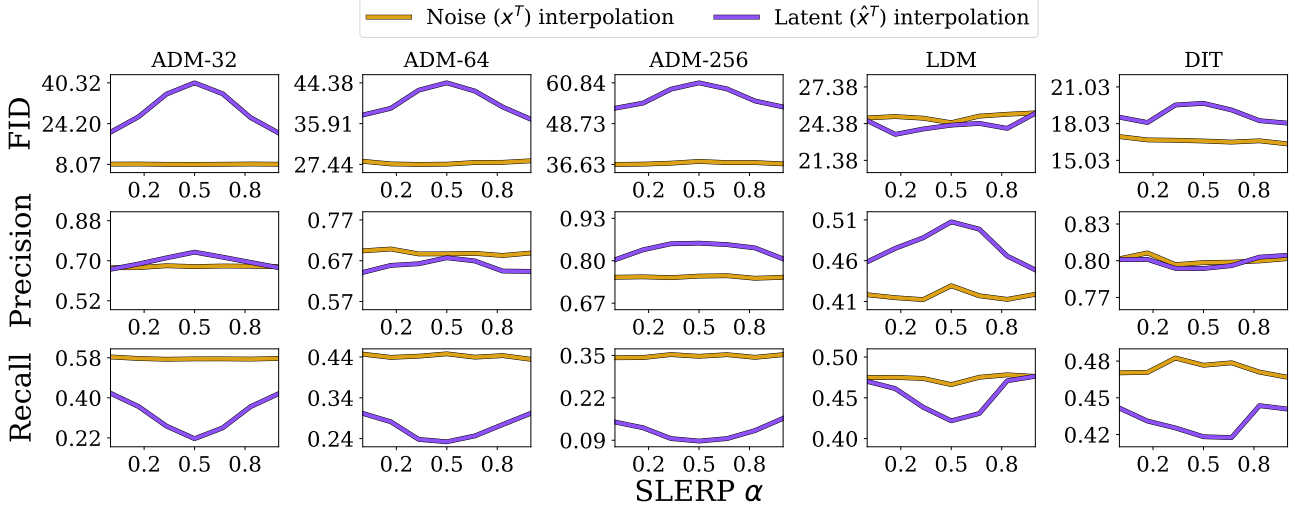


Figure 5. **The quality of images generated from spherical linear interpolations of latents  $\hat{x}_T$  deteriorates along the interpolation path, as indicated by the FID peak in the middle.** In contrast, the quality of generations from noise  $x_T$  interpolations remains stable. Recall metric reveal that the use of latent interpolation leads to the generation of much less diverse than noise.

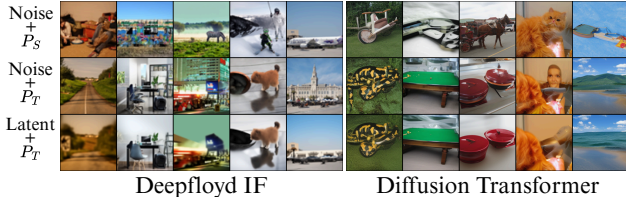


Figure 6. **Uniform regions in the images, encoded in the latents, reduce diversity in the generations when starting from inverse DDIM latents (third row) with different conditioning prompts.** In contrast, using clean noise as the starting point (second row) leads to more diverse outputs.

Using source prompts  $P_S$ , we generate images  $I_S$  from Gaussian noise  $x_T$  and invert them back into the latents  $\hat{x}_T$ . Next, we regenerate images  $\hat{I}_T$  from the latents, changing the conditioning to the target prompts  $P_T$ . As the ground truth regenerations  $I_T$ , we generate images from the original noise  $x_T$  with target prompts  $P_T$ . In Fig. 6, we present the drawback of leveraging latent variables as starting points for the denoising, where the  $I_S$  images’ structures in the latents limit editing performance at those locations in  $\hat{I}_T$  images.

In Tab. 7, we quantitatively measure this effect. First, we calculate the diversity of target generations ( $I_T, \hat{I}_T$ ) against source images ( $I_S$ ). We use DreamSim distance [9], LPIPS [56], SSIM [51], and cosine similarity of DINO features [5] to measure the distance between two sets of generations. The experiment shows that edits resulting from latent encodings  $\hat{I}_T$  are characterized by higher similarity (SSIM, DINO) and lower diversity (DreamSim, LPIPS) relative to starting images  $I_S$  than the one resulting from noises  $I_T$ . At the same time, in the bottom rows of Tab. 7, we show that the correlations occurring in the latent encodings induce lower performance in text-alignment to target prompts  $P_T$ , which we measure by calculating cosine similarity between text

Property	Metric	DiT		Deepfloyd IF	
		Noise $x_T$	Latent $\hat{x}_T$	Noise $x_T$	Latent $\hat{x}_T$
Diversity against $I_S$	DreamSim $\uparrow$	0.71 $\pm$ 0.12	0.69 $\pm$ 0.13	0.67 $\pm$ 0.10	0.64 $\pm$ 0.11
	LPIPS $\uparrow$	0.59 $\pm$ 0.12	0.57 $\pm$ 0.12	0.39 $\pm$ 0.11	0.36 $\pm$ 0.11
	SSIM $\downarrow$	0.23 $\pm$ 0.13	0.25 $\pm$ 0.14	0.31 $\pm$ 0.15	0.35 $\pm$ 0.15
	DINO $\downarrow$	0.17	0.20	0.33	0.38
Text alignment	CLIP-T ( $P_S$ ) $\downarrow$	0.456	0.543	0.0	0.0
	CLIP-T ( $P_T$ ) $\uparrow$	0.689	0.568	0.0	0.0

Table 7. **Diversity in relation to source images  $I_S$  and prompt alignment for generations from noise  $x_T$  and latents  $\hat{x}_T$ , conditioned on target prompt.** The arrows ( $\uparrow/\downarrow$ ) indicate greater generation diversity and higher text alignment to the target prompt.

embeddings and resulting image embeddings, both obtained with the CLIP [38] encoder. For the DiT model, our experiment indicates that generations from latents are as similar to the target prompt from the regeneration as to the source prompt used only during the inversion procedure.

### 4.3. Noise-to-sample vs. latent-to-sample mapping

As indicated by previous works [19, 54], diffusion models converge to the same mapping between the random Gaussian noise ( $x_T$ ) and the generated images ( $x_0$ ) independently on the random seed, parts of the dataset, or even the model architecture. We further investigate this property from the noise-to-sample and sample-to-latent mapping perspective.

We generate 2K samples from Gaussian noise, and for a given noise  $x_T$ , we predict the resulting generation  $x_0$  (and vice versa) by calculating its  $l_2$ -distance to all the images and selecting the closest one. We provide more details on the assignment procedure in Appendix E.1.

In Tab. 8, we show that it is possible to accurately assign the starting noises to the corresponding image generations ( $x_0 \rightarrow x_T$ ) for pixel diffusion models, while reverse assignment ( $x_T \rightarrow x_0$ ) is not possible. In Appendix E.3, we explain that assigning images to the noise is unfeasible be-

Model	Noise-Image Assignment		Latent-Image Assignment	
	$\mathbf{x}_0 \rightarrow \mathbf{x}_T$	$\mathbf{x}_T \rightarrow \mathbf{x}_0$	$\mathbf{x}_0 \rightarrow \hat{\mathbf{x}}_T$	$\hat{\mathbf{x}}_T \rightarrow \mathbf{x}_0$
ADM-32	98.9 $\pm$ 1.2	50.4 $\pm$ 1.9	16.4 $\pm$ 6.1	33.4 $\pm$ 2.7
ADM-64	100 $\pm$ 0.0	59.0 $\pm$ 7.1	8.6 $\pm$ 9.3	57.5 $\pm$ 7.3
ADM-256	100 $\pm$ 0.0	23.2 $\pm$ 4.8	4.1 $\pm$ 1.4	23.9 $\pm$ 5.0
IF	99.8 $\pm$ 0.2	52.6 $\pm$ 5.9	3.1 $\pm$ 1.8	50.0 $\pm$ 5.6
LDM	100 $\pm$ 0.0	100 $\pm$ 0.0	100 $\pm$ 0.0	100 $\pm$ 0.0
DiT	100 $\pm$ 0.0	90.7 $\pm$ 10.1	99.5 $\pm$ 1.7	90.7 $\pm$ 10.3

Table 8. Accuracy on assigning noise or inverted latent encoding to the generated image and vice versa. For pixel DMs, assigning starting noise to the generated images can be done by selecting the closest one with  $l_2$  distance, while other assignments are impossible. For latent-space models (LDM and DiT), all the assignments can be done using the L2 distance. In Appendix E.2, we present that this property holds for different numbers of steps  $T$ .

cause of the singular generations with low pixel variance, which are the closest for most of the noises. This fact, connected with the findings on reduced diversity of latents, suggests that latents, unlike noise, cannot be accurately assigned to samples, as evidenced by Tab. 8. It shows that latents significantly differ from noise in their mapping to images.

## 5. On the effect of the first inversion steps

Building on our prior findings, which indicate that initial inversion steps predominantly contribute to the divergence between latent variables and Gaussian noise, we conclude the experiments with an evaluation of how we could mitigate those issues with access to ground truth inversion steps.

To this end, we generate  $N = 10000$  images with  $T = 50$  diffusion steps with DiT and IF models and, similarly as in Sec. 3.4, we substitute intermediate noise predictions  $\{\mathcal{E}_t^S\}_{t=50\dots 1}$  during sampling.

First, in Tab. 9, we show that by replacing the approximations of the model’s predictions only for the first 5 inversion steps (10%) with the ground truth ones, we obtain the latent variables with less than 50%, for DiT, and less than 15%, for IF, pixel correlation compared to standard latents. This reduction of less diverse areas in latents comes along with a decrease in the noise reconstruction error, calculated as  $l_2$  distance  $\frac{1}{N} \sum_i \|x_T^{[i]} - \hat{x}_T^{[i]}\|_2$ , and Kullback–Leibler (KL) divergence to the Gaussian noise. However, it does not affect the image reconstruction.

Next, we evaluate how replacing the diffusion model’s predictions affects the diversity and text alignment of generated outputs. As shown in Fig. 7 for IF, swapping DM’s approximated predictions with denoising outputs during the first 3 inversion steps reduces the difference in diversities for images resulting from latents and those generated from noise by 50%. This reduction is observed across both distance-based metrics (DreamSim, LPIPS) and similarity-based metrics (SSIM, DINO). Additionally, in Fig. 7, we show for both models that replacing the first 3 DM predictions during inversion results in a significant decrease in modified

Inversion predictions replaced (% $T$ )	DiT				IF			
	Pixel Corr.	Reconstruction Image	Noise	KL Div. $\mathcal{N}(0; T)$	Pixel Corr.	Reconstruction Image	Noise	KL Div. $\mathcal{N}(0; T)$
$\emptyset$ (0%)	0.16	0.05	0.15	0.011	0.64	0.07	0.55	0.60
1 (2%)	0.16	0.05	0.15	0.011	0.61	0.07	0.51	0.56
1...3 (6%)	0.10	0.05	0.08	0.004	0.15	0.07	0.19	0.06
1...5 (10%)	0.07	0.05	0.06	0.002	0.09	0.07	0.12	0.03
1...10 (20%)	0.04	0.05	0.03	0.001	0.05	0.07	0.07	0.01
Noise (100%)	0.04	0.0	0.0	0.0	0.05	0.0	0.0	0.0

Table 9. Impact of DDIM Inversion approximation error in the first steps of the noising process on latent correlations, reconstruction errors, and the KL divergence between inversions and Gaussian noise. By starting the inversion procedure after 10% of the image corruption process, we significantly remove image structures from latents and drastically reduce their divergence from noise.

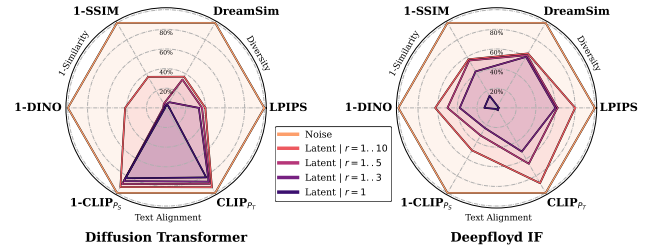


Figure 7. Impact of first DDIM inversion errors on latent generations’ diversity and text-alignment. For IF model (right), replacing the first inversion steps (denoted as  $r$ ) and denoising with a different prompt leads to more diverse generations against the source images  $I_S$ . For DiT (left), we show that replacing increases generations’ alignment to the target prompts, as indicated by the larger CLIP-T value for  $P_T$  and the smaller one for  $P_S$ . We present details of the experiment in Appendix F.2.

generations alignment to the source prompt ( $P_S$ ).

In Appendix F.1, we show that replacing predictions in the first 3% of steps also noticeably improves the quality of images generated from interpolations of final latents.

## 6. Conclusions

In this work, we analyze how errors introduced by the DDIM inversion algorithm influence the properties of latent image representations. Our findings reveal that the inverted latents exhibit systematic deviations from a Gaussian distribution, particularly in regions corresponding to smooth image surfaces. We trace this effect to the higher inversion error in these areas, which predominantly arise during the early noising steps. This discrepancy leads to practical limitations such as reduced diversity and lower text alignment to the conditioning prompts, or worse quality interpolation and editing in situations where latents are used as a starting point of the diffusion process. Our conclusions suggest that reducing the error difference for plain and non-plain image surfaces during the first inversion steps could mitigate these constraints, enhancing the usability of latents in generative applications and pointing additional direction for future research.

## References

- [1] Erik Bodin, Alexandru I. Stere, Dragos D Margineantu, Carl Henrik Ek, and Henry Moss. Linear combinations of latents in generative models: subspaces and beyond. In *The Thirteenth International Conference on Learning Representations*, 2025. 6
- [2] Manuel Brack, Felix Friedrich, Katharina Kornmeier, Linoy Tsaban, Patrick Schramowski, Kristian Kersting, and Apolinário Passos. Ledits++: Limitless image editing using text-to-image models. *CVPR*, 2024. 2, 3, 12
- [3] Duygu Ceylan, Chun-Hao P. Huang, and Niloy J. Mitra. Pix2video: Video editing using image diffusion. In *Proceedings of the IEEE/CVF International Conference on Computer Vision (ICCV)*, pages 23206–23217, 2023. 2
- [4] Hansam Cho, Jonghyun Lee, Seung Bum Kim, Tae-Hyun Oh, and Yonghyun Jeong. Noise map guidance: Inversion with spatial context for real image editing. In *The Twelfth International Conference on Learning Representations*, 2024. 2
- [5] Timothée Darcet, Maxime Oquab, Julien Mairal, and Piotr Bojanowski. Vision transformers need registers. In *The Twelfth International Conference on Learning Representations, ICLR 2024, Vienna, Austria, May 7-11, 2024*. OpenReview.net, 2024. 7
- [6] Kamil Deja, Georgi Tinchev, Marta Czarnowska, Marius Cotescu, and Jasha Droppo. Diffusion-based accent modelling in speech synthesis. In *Interspeech 2023*, 2023. 2
- [7] Prafulla Dhariwal and Alexander Nichol. Diffusion models beat GANs on image synthesis. *Advances in Neural Information Processing Systems*, 34, 2021. 1, 2, 3, 6, 12
- [8] Wenkai Dong, Song Xue, Xiaoyue Duan, and Shumin Han. Prompt tuning inversion for text-driven image editing using diffusion models. In *Proceedings of the IEEE/CVF International Conference on Computer Vision*, pages 7430–7440, 2023. 2, 12
- [9] Stephanie Fu, Netanel Tamir, Shobhita Sundaram, Lucy Chai, Richard Zhang, Tali Dekel, and Phillip Isola. Dreamsim: Learning new dimensions of human visual similarity using synthetic data. In *Advances in Neural Information Processing Systems*, pages 50742–50768, 2023. 7
- [10] Daniel Garibi, Or Patashnik, Andrey Voynov, Hadar Averbuch-Elor, and Daniel Cohen-Or. Renoise: Real image inversion through iterative noising. *arXiv preprint arXiv:2403.14602*, 2024. 1, 2, 3, 6, 12
- [11] Ligong Han, Song Wen, Qi Chen, Zhixing Zhang, Kunpeng Song, Mengwei Ren, Ruijiang Gao, Anastasis Stathopoulos, Xiaoxiao He, Yuxiao Chen, et al. Proxedit: Improving tuning-free real image editing with proximal guidance. In *Proceedings of the IEEE/CVF Winter Conference on Applications of Computer Vision*, pages 4291–4301, 2024. 2
- [12] Amir Hertz, Ron Mokady, J. Tenenbaum, Kfir Aberman, Y. Pritch, and D. Cohen-Or. Prompt-to-prompt image editing with cross attention control. *International Conference on Learning Representations*, 2022. 2, 6, 12
- [13] Jonathan Ho and Tim Salimans. Classifier-free diffusion guidance. In *NeurIPS 2021 Workshop on Deep Generative Models and Downstream Applications*, 2021. 2
- [14] Jonathan Ho, Ajay Jain, and Pieter Abbeel. Denoising diffusion probabilistic models. In *Advances in Neural Information Processing Systems*, pages 6840–6851. Curran Associates, Inc., 2020. 2, 12
- [15] Jonathan Ho, William Chan, Chitwan Saharia, Jay Whang, Ruiqi Gao, Alexey Gritsenko, Diederik P Kingma, Ben Poole, Mohammad Norouzi, David J Fleet, et al. Imagen video: High definition video generation with diffusion models. *arXiv preprint arXiv:2210.02303*, 2022. 1
- [16] Seongmin Hong, Kyeonghyun Lee, Suh Yoon Jeon, Hyewon Bae, and Se Young Chun. On exact inversion of dpm-solvers. In *Proceedings of the IEEE/CVF Conference on Computer Vision and Pattern Recognition*, pages 7069–7078, 2024. 1, 2, 3, 12
- [17] Inbar Huberman-Spiegelglas, Vladimir Kulikov, and Tomer Michaeli. An edit friendly ddpm noise space: Inversion and manipulations. In *Proceedings of the IEEE/CVF Conference on Computer Vision and Pattern Recognition*, pages 12469–12478, 2024. 1, 3, 6, 12
- [18] Xuan Ju, Ailing Zeng, Yuxuan Bian, Shaoteng Liu, and Qiang Xu. Pnp inversion: Boosting diffusion-based editing with 3 lines of code. In *The Twelfth International Conference on Learning Representations*, 2024. 2
- [19] Zahra Kadhodaie, Florentin Guth, Eero P. Simoncelli, and Stéphane Mallat. Generalization in diffusion models arises from geometry-adaptive harmonic representations. In *The Twelfth International Conference on Learning Representations, ICLR 2024, Vienna, Austria, May 7-11, 2024*. OpenReview.net, 2024. 3, 7
- [20] Valentin Khruikov and I. Oseledets. Understanding ddpm latent codes through optimal transport. *International Conference on Learning Representations*, 2022. 3
- [21] Gwanghyun Kim, Taesung Kwon, and Jong Chul Ye. Diffusionclip: Text-guided diffusion models for robust image manipulation. In *Proceedings of the IEEE/CVF Conference on Computer Vision and Pattern Recognition (CVPR)*, pages 2426–2435, 2022. 2
- [22] Young-Heon Kim and E. Milman. A generalization of caffarelli’s contraction theorem via (reverse) heat flow. *Mathematische Annalen*, 2011. 3
- [23] Diederik P. Kingma and Max Welling. Auto-Encoding Variational Bayes. In *International Conference on Learning Representations*, 2014. 1
- [24] Tuomas Kynkäänniemi, Tero Karras, Samuli Laine, Jaakko Lehtinen, and Timo Aila. Improved precision and recall metric for assessing generative models. *Advances in neural information processing systems*, 32, 2019. 6
- [25] Hugo Lavenant and Filippo Santambrogio. The flow map of the fokker–planck equation does not provide optimal transport. *Applied Mathematics Letters*, 133:108225, 2022. 3
- [26] Xianhang Li, Haoqin Tu, Mude Hui, Zeyu Wang, Bingchen Zhao, Junfei Xiao, Sucheng Ren, Jieru Mei, Qing Liu, Huangjie Zheng, Yuyin Zhou, and Cihang Xie. What if we recaption billions of web images with llama-3? *arXiv preprint arXiv:2406.12345*, 2024. 3, 6
- [27] Haonan Lin, Mengmeng Wang, Jiahao Wang, Wenbin An, Yan Chen, Yong Liu, Feng Tian, Guang Dai, Jingdong Wang,

- and Qianying Wang. Schedule your edit: A simple yet effective diffusion noise schedule for image editing. *Neural Information Processing Systems*, 2024. 2, 3
- [28] Jinglin Liu, Chengxi Li, Yi Ren, Feiyang Chen, and Zhou Zhao. Diffsinger: Singing voice synthesis via shallow diffusion mechanism. *AAAI Conference on Artificial Intelligence*, 2021. 1
- [29] Barak Meiri, Dvir Samuel, Nir Darshan, Gal Chechik, Shai Avidan, and Rami Ben-Ari. Fixed-point inversion for text-to-image diffusion models. *arXiv preprint arXiv:2312.12540*, 2023. 1, 2, 12
- [30] Chenlin Meng, Yutong He, Yang Song, Jiaming Song, Jiajun Wu, Jun-Yan Zhu, and Stefano Ermon. Sdedit: Guided image synthesis and editing with stochastic differential equations. In *The Tenth International Conference on Learning Representations, ICLR 2022, Virtual Event, April 25-29, 2022*. OpenReview.net, 2022. 12
- [31] Daiki Miyake, Akihiro Iohara, Yu Saito, and Toshiyuki Tanaka. Negative-prompt inversion: Fast image inversion for editing with text-guided diffusion models. *arXiv preprint arXiv: 2305.16807*, 2023. 2, 12
- [32] Ron Mokady, Amir Hertz, Kfir Aberman, Yael Pritch, and Daniel Cohen-Or. Null-text inversion for editing real images using guided diffusion models. In *Proceedings of the IEEE/CVF Conference on Computer Vision and Pattern Recognition (CVPR)*, pages 6038–6047, 2023. 1, 2, 3, 6, 12
- [33] Alexander Quinn Nichol and Pratul Dhariwal. Improved denoising diffusion probabilistic models. In *International conference on machine learning*, pages 8162–8171. PMLR, 2021. 17
- [34] Zhihong Pan, Riccardo Gherardi, Xiufeng Xie, and Stephen Huang. Effective real image editing with accelerated iterative diffusion inversion. In *Proceedings of the IEEE/CVF International Conference on Computer Vision (ICCV)*, pages 15912–15921, 2023. 2, 12
- [35] Gaurav Parmar, Krishna Kumar Singh, Richard Zhang, Yijun Li, Jingwan Lu, and Jun-Yan Zhu. Zero-shot image-to-image translation. In *ACM SIGGRAPH 2023 Conference Proceedings*, pages 1–11, 2023. 1, 2, 3, 12
- [36] William Peebles and Saining Xie. Scalable diffusion models with transformers. In *Proceedings of the IEEE/CVF International Conference on Computer Vision (ICCV)*, pages 4195–4205, 2023. 3, 6
- [37] Vadim Popov, Ivan Vovk, Vladimir Gogoryan, Tasnima Sadekova, and Mikhail Kudinov. Grad-tts: A diffusion probabilistic model for text-to-speech. In *International Conference on Machine Learning*, pages 8599–8608. PMLR, 2021. 1
- [38] Alec Radford, Jong Wook Kim, Chris Hallacy, A. Ramesh, Gabriel Goh, Sandhini Agarwal, Girish Sastry, Amanda Askell, Pamela Mishkin, Jack Clark, Gretchen Krueger, and Ilya Sutskever. Learning transferable visual models from natural language supervision. In *ICML*, 2021. 7
- [39] Robin Rombach, A. Blattmann, Dominik Lorenz, Patrick Esser, and B. Ommer. High-resolution image synthesis with latent diffusion models. *Computer Vision and Pattern Recognition*, 2021. 3, 15
- [40] Litu Rout, Yujia Chen, Nataniel Ruiz, Constantine Caramanis, Sanjay Shakkottai, and Wen-Sheng Chu. Semantic image inversion and editing using rectified stochastic differential equations. In *The Thirteenth International Conference on Learning Representations*, 2025. 12
- [41] Dvir Samuel, Rami Ben-Ari, Nir Darshan, Haggai Maron, and Gal Chechik. Norm-guided latent space exploration for text-to-image generation. *Advances in Neural Information Processing Systems*, 36:57863–57875, 2023. 6, 12
- [42] Ken Shoemake. Animating rotation with quaternion curves. In *Proceedings of the 12th Annual Conference on Computer Graphics and Interactive Techniques*, page 245–254, New York, NY, USA, 1985. Association for Computing Machinery. 6
- [43] Jascha Sohl-Dickstein, Eric Weiss, Niru Maheswaranathan, and Surya Ganguli. Deep unsupervised learning using nonequilibrium thermodynamics. In *International Conference on Machine Learning*, pages 2256–2265. PMLR, 2015. 1
- [44] Jiaming Song, Chenlin Meng, and Stefano Ermon. Denoising diffusion implicit models. *arXiv preprint arXiv:2010.02502*, 2020. 1, 2, 6, 12
- [45] Yang Song, Jascha Sohl-Dickstein, Diederik P. Kingma, Abhishek Kumar, Stefano Ermon, and Ben Poole. Score-based generative modeling through stochastic differential equations. In *9th International Conference on Learning Representations, ICLR 2021, Virtual Event, Austria, May 3-7, 2021*. OpenReview.net, 2021. 4
- [46] StabilityAI. DeepFloyd IF: a novel state-of-the-art open-source text-to-image model with a high degree of photorealism and language understanding. <https://github.com/deep-floyd/IF>, 2023. Retrieved on 2023-04-17. 3, 6
- [47] Xu Su, Jiaming Song, Chenlin Meng, and Stefano Ermon. Dual diffusion implicit bridges for image-to-image translation. *International Conference on Learning Representations*, 2022. 2
- [48] Chuanming Tang, Kai Wang, and Joost van de Weijer. IterInv: Iterative Inversion for Pixel-Level T2I Models. In *2024 IEEE International Conference on Multimedia and Expo (ICME)*, pages 1–6, Los Alamitos, CA, USA, 2024. IEEE Computer Society. 2, 12
- [49] Bram Wallace, Akash Gokul, and Nikhil Naik. Edict: Exact diffusion inversion via coupled transformations. In *Proceedings of the IEEE/CVF Conference on Computer Vision and Pattern Recognition*, pages 22532–22541, 2023. 3, 12
- [50] Fangyikang Wang, Hubery Yin, Yuejiang Dong, Huminhao Zhu, Chao Zhang, Han Zhao, Hui Qian, and Chen Li. Belm: Bidirectional explicit linear multi-step sampler for exact inversion in diffusion models. *Neural Information Processing Systems*, 2024. 2
- [51] Zhou Wang, Alan C Bovik, Hamid R Sheikh, and Eero P Simoncelli. Image quality assessment: from error visibility to structural similarity. *IEEE transactions on image processing*, 13(4):600–612, 2004. 7
- [52] George Wolberg. Image morphing: a survey. *The visual computer*, 14(8-9):360–372, 1998. 6
- [53] Guanhua Zhang, Jiabao Ji, Yang Zhang, Mo Yu, Tommi S. Jaakkola, and Shiyu Chang. Towards coherent image inpaint-

- ing using denoising diffusion implicit models. In *International Conference on Machine Learning, ICML 2023, 23-29 July 2023, Honolulu, Hawaii, USA*, pages 41164–41193. PMLR, 2023. [2](#)
- [54] Huijie Zhang, Jinfan Zhou, Yifu Lu, Minzhe Guo, Liyue Shen, and Qing Qu. The emergence of reproducibility and consistency in diffusion models, 2024. [3](#), [7](#)
- [55] Kaiwen Zhang, Yifan Zhou, Xudong Xu, Bo Dai, and Xingang Pan. Diffmorpher: Unleashing the capability of diffusion models for image morphing. In *Proceedings of the IEEE/CVF Conference on Computer Vision and Pattern Recognition*, pages 7912–7921, 2024. [6](#), [12](#)
- [56] Richard Zhang, Phillip Isola, Alexei A Efros, Eli Shechtman, and Oliver Wang. The unreasonable effectiveness of deep features as a perceptual metric. In *CVPR*, 2018. [7](#)
- [57] Yuechen Zhang, Jinbo Xing, Eric Lo, and Jiaya Jia. Real-world image variation by aligning diffusion inversion chain. In *Advances in Neural Information Processing Systems*, pages 30641–30661. Curran Associates, Inc., 2023. [2](#)
- [58] PengFei Zheng, Yonggang Zhang, Zhen Fang, Tongliang Liu, Defu Lian, and Bo Han. Noisediffusion: Correcting noise for image interpolation with diffusion models beyond spherical linear interpolation. In *The Twelfth International Conference on Learning Representations*, 2024. [1](#), [2](#), [6](#), [12](#)

# There and Back Again: On the relation between Noise and Image Inversions in Diffusion Models

## Supplementary Material

### A. On approximation error in DDIM Inversion

Denosing Diffusion Probabilistic Models (DDPMs [14]) generate samples by reversing the forward diffusion process, modeled as a Markov Chain, where a clean image  $x_0$  is progressively transformed to white Gaussian noise  $x_T$  in  $T$  diffusion steps. A partially noised image  $x_t$ , which serves as an intermediate object in this process, is expressed as

$$x_t = \sqrt{\bar{\alpha}_t}x_0 + \sqrt{1 - \bar{\alpha}_t}\epsilon_t, \quad (7)$$

where  $\bar{\alpha}_t = \prod_{s=1}^t \alpha_s$ ,  $\alpha_t = 1 - \beta_t$ ,  $\epsilon_t \sim \mathcal{N}(0, \mathcal{I})$ , and  $\{\beta_t\}_{t=1}^T$  is a variance schedule, controlling how much of the noise is contained in the image at the specific step  $t$ .

To enable sampling clean images from clean Gaussian noises, the neural network  $\epsilon_\theta$  is trained to predict the noise added to a clean image  $x_0$  for a given intermediate image  $x_t$ . Such a trained model is further utilized in the backward diffusion process by iteratively transferring a more noisy image ( $x_t$ ) to the less noisy one ( $x_{t-1}$ ) as

$$x_{t-1} = \frac{1}{\sqrt{\alpha_t}}(x_t - \frac{\beta_t}{\sqrt{1 - \bar{\alpha}_t}}\epsilon_\theta^{(t)}(x_t)) + \sigma_t z, \quad (8)$$

with  $z \sim \mathcal{N}(0, \mathcal{I})$  being a noise portion added back for denoising controlled by  $\sigma_t = \sqrt{\beta_t(1 - \bar{\alpha}_{t-1})/(1 - \bar{\alpha}_t)}$ .

Song et al. [44] reformulate the diffusion process as a non-Markovian, which leads to a speed-up of the sampling process. While previously obtaining a less noisy image at  $x_t$  required all past denoising steps from  $T$  till  $(t + 1)$ , this approach allows skipping some steps during sampling. More precisely, the backward diffusion process is defined as a combination of predictions of image  $x_0$ , next denoising step

$x_t$ , and random noise:

$$x_{t-1} = \sqrt{\bar{\alpha}_{t-1}} \left( \frac{x_t - \sqrt{1 - \bar{\alpha}_t} \epsilon_\theta^{(t)}(x_t)}{\sqrt{\bar{\alpha}_t}} \right) + \sqrt{1 - \bar{\alpha}_{t-1} - \sigma_t^2} \cdot \epsilon_\theta^{(t)}(x_t) + \sigma_t z_t \quad (9)$$

with  $\sigma_t = \eta \sqrt{\beta_t(1 - \bar{\alpha}_{t-1})/(1 - \bar{\alpha}_t)}$ , and  $z_t \sim \mathcal{N}(0, \mathcal{I})$ .

While setting  $\eta = 1$  makes Eq. (9) equivalent to Eq. (8), leading to a Markovian probabilistic diffusion model, setting  $\eta = 0$  removes the random component from the equation, making it a Denoising Diffusion Implicit Model (DDIM), which prominent ability is to perform a deterministic mapping from given noise ( $x_T$ ) to image ( $x_0$ ). One of the potential benefits of implicit models is the possibility of reversing the backward diffusion process to transfer images back to the original noise. Operating in such a space by modifying resulting inversions unlocks numerous image manipulation capabilities, i.e., image editing [2, 8, 10, 12, 16, 17, 29, 31, 32, 34, 35, 40, 48, 49], image interpolation [7, 41, 55, 58], or stroke-to-image synthesis [30, 40]. The inversion process can be derived from Eq. (9), leading to the formula for transferring a less noisy image  $x_{t-1}$  to a more noisy one  $x_t$ :

$$x_t = \sqrt{\alpha_t}x_{t-1} + (\sqrt{1 - \bar{\alpha}_t} - \sqrt{\alpha_t - \bar{\alpha}_t}) \cdot \epsilon_\theta^{(t)}(x_t) \quad (10)$$

Unfortunately, a perfect image-to-noise inversion is infeasible. Due to circular dependency on  $x_t$  within Eq. (10), Dhariwal and Nichol [7] propose to approximate this equation by assuming that the model’s prediction in  $t$ -th step is locally equivalent to the decision in  $(t - 1)$ -th step  $\epsilon_\theta^{(t)}(x_t) \approx \epsilon_\theta^{(t)}(x_{t-1})$ . The inverted trajectory is determined in multiple steps. Hence, the error propagates further away from the image, leading to the latents that deviate from the starting noise. This flaw is presented in Fig. 8.

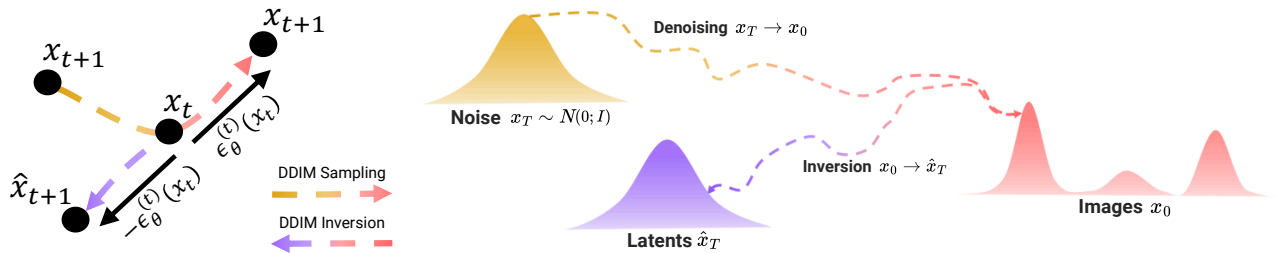


Figure 8. The DDIM inversion error, derived from approximating DM’s prediction in step  $t$  with the  $(t + 1)$  output (left), propagates with the next inversion steps, leading to a distribution of latents  $\hat{x}^T$  that deviates significantly from the expected noise distribution  $x^T$  (right).

## B. Most probable triangles

In Sec. 3.3, we analyze where the latent encodings are distributed in relation to the initial noise and generated samples. In this section, we describe the methodology for obtaining such triangles, as well as investigate how those relations change depending on a number of diffusion steps  $T$ .

### B.1. Methodology

First, we determine the vectors going from each vertex to the other vertices of the noise-sample-latent ( $x_T$ - $x_0$ - $\hat{x}_T$ ) triangle. For sample  $x_0$ , we obtain a vector leading to noise  $\overrightarrow{x_0 x_T} = x_T - x_0$  and to latent  $\overrightarrow{x_0 \hat{x}_T} = \hat{x}_T - x_0$ , and calculate the angle between them using cosine similarity as

$$\angle_{x_0} = \arccos \frac{\overrightarrow{x_0 x_T} \cdot \overrightarrow{x_0 \hat{x}_T}}{\|\overrightarrow{x_0 x_T}\| \|\overrightarrow{x_0 \hat{x}_T}\|}, \quad (11)$$

and convert resulting radians to degrees. Similarly, we obtain the angle next to the noise  $\angle_{x_T}$  and latent  $\angle_{\hat{x}_T}$ .

Next, we determine histograms for each angle, approximating the probability density function for every angle ( $p_{\angle_{x_T}}, p_{\angle_{x_0}}, p_{\angle_{\hat{x}_T}}$ ) binned up to the precision of one degree, see Fig. 9. Finally, for all angles triples candidates (where  $\angle_{x_T} + \angle_{x_0} + \angle_{\hat{x}_T} = 180^\circ$ ), we calculate the probability of a triangle as the product of the probabilities and choose the triplet maximizing such joint probability:

$$\operatorname{argmax}_{(\angle_{x_T}, \angle_{x_0}, \angle_{\hat{x}_T})} p_{\angle_{x_T}} \cdot p_{\angle_{x_0}} \cdot p_{\angle_{\hat{x}_T}}. \quad (12)$$

In Fig. 9, we provide example triangles for ADM-32 (a), ADM-256 (b), and LDM (c), which we calculate using  $N = 1000$  images with  $T = 100$  diffusion steps.

### B.2. Impact of T on noise-image-latent triangles

Additionally, in Tab. 10 we show how the relations change when sampling and inversion is done for variant  $T$ .

Model	$T$	$\angle_{x_0}$	$\angle_{x_T}$	$\angle_{\hat{x}_T}$
ADM 32 × 32	10	44	16	120
	100	29	28	123
	1000	20	45	115
ADM 64 × 64	10	30	31	119
	100	11	60	109
	1000	6	79	95
ADM 256 × 256	10	24	50	106
	100	24	73	83
	1000	23	73	84
LDM 256 × 256	10	23	53	104
	100	2	76	102
	1000	1	83	96
DiT 256 × 256	10	27	47	106
	100	4	66	110
	1000	1	80	99

Table 10. **Impact of the number of diffusion steps  $T$  on angles in the noise  $x_T$ , image  $x_0$ , and latent  $\hat{x}_T$  triangle.** Regardless of the number of diffusion steps, latents appear between Gaussian noise and generations.

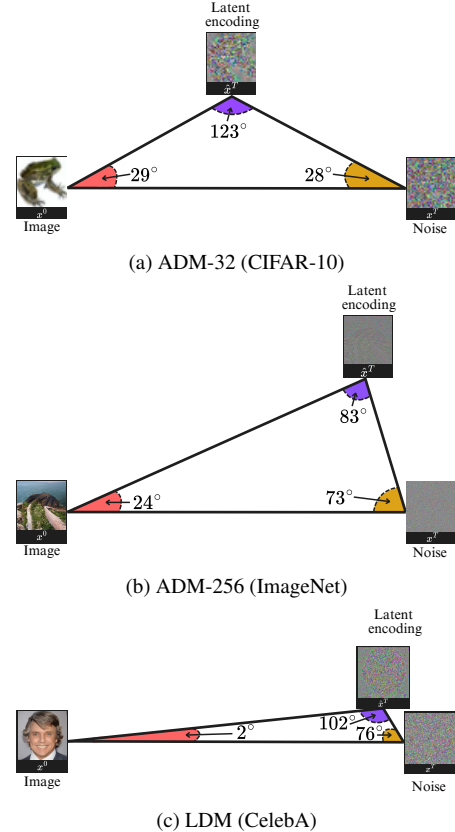


Figure 9. **Most probable triangles formed from random Gaussian noise ( $x_T$ ), the images ( $x_0$ ) generated, and latents ( $\hat{x}_T$ ) recovered with DDIM Inversion procedure.**

### B.3. Example histograms

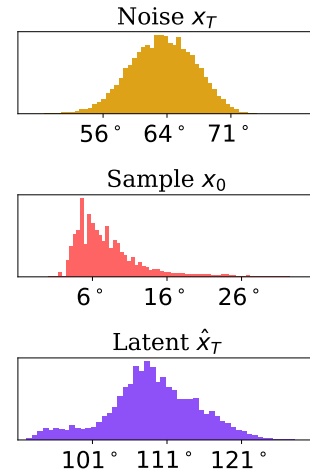


Figure 10. **Histograms approximating probability density functions of angles values for noise, sample, and latent vertices.** Example calculated for DiT model using  $T = 100$  diffusion steps.

### C. Plain surface thresholding

During our experiments, we determine binary mask  $\mathcal{M}$  to identify pixels corresponding to the plain areas in the images. We describe this process in this section.

Let  $\mathbf{I} \in \mathbb{R}^{C \times H \times W}$  be the input image. For each pixel value across every channel  $(c, h, w)$  in  $\mathbf{I}$ , we compute the absolute difference to point in the next row  $D_H(c, h, w) = |I_{c,h+1,w} - I_{c,h,w}|$  and to the pixel in the next column  $D_W(c, h, w) = |I_{c,h,w+1} - I_{c,h,w}|$ . We obtain  $D_H \in \mathbb{R}^{C \times H-1 \times W}$  and  $D_W \in \mathbb{R}^{C \times H \times W-1}$ , which we pad with zeros (last row for  $D_H$  and last column for  $D_W$ ), making them of shape  $C \times H \times W$ . The difference matrix  $D$ , representing how a point varies from its neighbors, is computed as  $D = (D_W + D_H)/2$ .

Finally, we determine a binary mask  $\mathcal{M}_c$  per each channel  $c$ , by applying threshold  $\tau$  to  $D$  as

$$\mathcal{M}_c(h, w) = \begin{cases} 1, & \text{if } D_c(h, w) < \tau \\ 0, & \text{otherwise} \end{cases} \quad (13)$$

During the experiments, we set  $\tau = 0.025$ .

The final mask  $\mathcal{M} \in \{0, 1\}^{W \times H}$  can be derived by evaluating the logical AND across all channels for each pixel location as

$$\mathcal{M}(h, w) = \prod_c \mathcal{M}_c(h, w). \quad (14)$$

After obtaining the final mask for plain pixels, which we denote as  $\mathcal{M}_p$ , the according mask for non-plain image surfaces can be obtained by applying logical NOT to the mask as  $\mathcal{M}_n = \neg \mathcal{M}_p$ . In Fig. 11, we present example masks determined using our methodology.

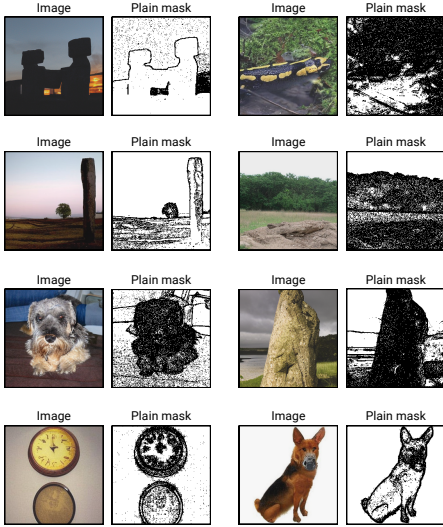


Figure 11. Examples of samples together with their masks indicating plain areas (white). Images generated using DiT model.

### D. Details on calculating inversion error

In Sec. 3.4, we study how the inversion error differs for pixels related to plain and non-plain samples' regions and investigate it across diffusion steps. In this section, we describe the method for determining the error.

First, we generate  $N = 4k$  images with  $T = 50$  diffusion steps with both ADM-64 and DiT models, saving intermediate noise predictions  $\{\mathcal{E}_t^S\}_{t=50 \dots 1}$  during sampling. Next, we collect diffusion model outputs during the inversion process  $\{\mathcal{E}_t^I\}_{t=1 \dots 50}$  assuming all the previous steps were correct. While for  $t = 1$ ,  $\mathcal{E}_1^I$  can be set to the diffusion model prediction from the first inversion step  $\epsilon_\theta(x_0)$ , for further steps, more advanced methodology is necessary. To this end, for each  $t' = 2 \dots 50$ , we map the images to latents with DDIM Inversion, replacing in  $t = 1 \dots t' - 1$  the predicted noise  $\epsilon_\theta(x_t)$  with the ground truth prediction  $\mathcal{E}_t^S$  from denoising process, and collect the model output for the  $t'$  step as  $\mathcal{E}_{t'}^I := \epsilon_\theta(x_{t'})$ . For step  $t$ , this methodology is equivalent to starting the inversion process from  $(t + 1)$  denoising step and collecting the first diffusion model prediction.

In the next step, we calculate the absolute error between outputs during inversion and ground truth predictions as  $\mathcal{E}_t^E = |\mathcal{E}_t^I - \mathcal{E}_t^S|$ . This way, we obtain the inversion approximation error for each timestep.

Further, for the images in the dataset, we obtain binary masks  $\mathcal{M}_p$  and  $\mathcal{M}_n$  indicating, respectively, plain ( $p$ ) and non-plain ( $n$ ) pixels in the image, according to the procedure described in Appendix C. To ensure that the level of noise that DM predicts in each step does not bias the results, we divide the absolute errors in each step by  $l_1$ -norm of model outputs, calculated separately for each diffusion step. For plain ( $p$ ) pixels, it can be described as

$$\mathcal{E}_t^{Ep} = 1/\|\mathcal{E}_t^I\|_1 \sum (\mathcal{E}_t^E \odot \mathcal{M}_p), \quad (15)$$

and adequately for non-plain ( $n$ ) pixels as

$$\mathcal{E}_t^{En} = 1/\|\mathcal{E}_t^I\|_1 \sum (\mathcal{E}_t^E \odot \mathcal{M}_n). \quad (16)$$

In Tab. 6, we present the error differences for plain and non-plain areas and how the first 10% of the diffusion steps contribute to the total inversion error. To calculate this error for plain regions in steps  $t_s, \dots, t_e$ , we sum errors for timesteps from a given interval as

$$\bar{\mathcal{E}}_{(t_s, t_e)}^{Ep} = \sum_{t'=t_s}^{t_e} \mathcal{E}_t^{Ep}. \quad (17)$$

## E. Noise-to-image mapping

In Sec. 4.3, we show that the mapping between output images and initial Gaussian noise can be realized through the closest  $l_2$ -distance assignment. In this section, we describe the experiment in detail, indicating this property independence from the number of diffusion steps  $T$  and explaining why it does not work in both directions.

### E.1. Smallest $l_2$ mapping

In our experimental setup, we sample  $N = 2000$  Gaussian noises and generate  $N$  corresponding images using a DDIM sampler. When predicting resulting images for the noises ( $\mathbf{x}_T \rightarrow \mathbf{x}_0$ ), we iterate over all the  $N$  noises, and for each of them, we calculate its pixel distances to all the  $N$  generations. For given noise, we select the image to which such  $l_2$ -distance is the smallest. Similarly, we investigate image-to-noise ( $\mathbf{x}_0 \rightarrow \mathbf{x}_T$ ), image-to-latent ( $\mathbf{x}_0 \rightarrow \hat{\mathbf{x}}_T$ ) and latent-to-image ( $\hat{\mathbf{x}}_T \rightarrow \mathbf{x}_0$ ) mappings.

During the experiment, we calculate the distance between two objects as  $l_2$  norm of the matrix of differences between them:  $\|x - y\|_2 = \sqrt{\sum_i^C \sum_j^H \sum_k^W (x_{i,j,k} - y_{i,j,k})^2}$ , where  $C \times H \times W$  are the dimensions of either pixel or latent space of diffusion model.

### E.2. Impact of the number of diffusion steps on the accuracy of the assignment

In Tab. 11, we investigate the accuracy of the procedure across varying numbers of diffusion steps  $T$  for both image $\leftrightarrow$ noise (a) and image $\leftrightarrow$ latent (b) assignments. We observe that assigning initial noise to generations through our distance method can be successfully done regardless of diffusion steps. For the reverse assignment, which is noise-to-image mapping, we can observe high accuracy with a low number of generation timesteps ( $T = 10$ ), but the results deteriorate quickly with the increase of this parameter. The reason for this is that greater values of  $T$  allow the generation of a broader range of images, including the ones with large plain areas of low pixel variance. When it comes to mappings between images and latents resulting from DDIM Inversion, assignment in both directions is infeasible for pixel diffusion, regardless of  $T$ . Additionally, both Gaussian noises  $x^T$  and latent encodings  $\hat{x}^T$ , that their assignment to images in both directions can be successfully performed when the denoising process is performed in the latent space, as shown for DiT and LDM models. We hypothesize that this fact is connected with the KL regularization term that imposes a slight penalty towards a standard normal distribution  $\mathcal{N}(0, I)$  on the learned latent during training [39]. In Appendix G.2, we show that the studied mapping between noise  $\mathbf{x}_T$  and samples  $\mathbf{x}_0$  is established at the beginning of diffusion model training.

## E.3. Asymmetry of Noise-to-Image mapping

Results in Tab. 11a indicate that, even though the  $l_2$ -distance is symmetrical, the mapping cannot be done in both directions. The reason behind this is that image and noise assignments are not the same due to the one-directional many-to-one relation, *e.g.*, there might be several noises pointing towards the same closest image.

We present examples of wrong noise-to-image ( $\mathbf{x}_T \rightarrow \mathbf{x}_0$ ) assignments in Fig. 12A for ADM-64. In Fig. 12B, we present the singular generations that lead to incorrect noise-to-image classification (noise attractors), along with the number of noises for which they are the closest. Interestingly, in Fig. 12C, we sort all the generations used in the experiment by the variance of pixels and show 8 least variant images. We observe that the set of singular generations leading to misclassification partially overlaps with lowest-variance generations. In Fig. 13 we observe similar properties for experiment with ADM-32 model.

When assigning images to the initial noises, there are singular generations (with large plain areas) located close to the mean of the random Gaussian noise in the set of generated images. Such generations tend to be the closest (in  $l_2$ -distance) for the majority of the noises in our experiments.

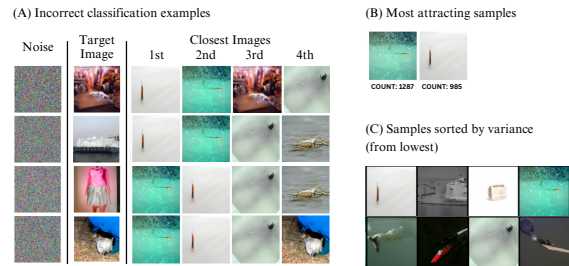


Figure 12. Examples of incorrect assignments of initial noises to resulting images (A), two most noise-attracting images (B), and samples sorted in ascending order by variance of pixels for ADM-64 model trained on the **ImageNet** dataset.

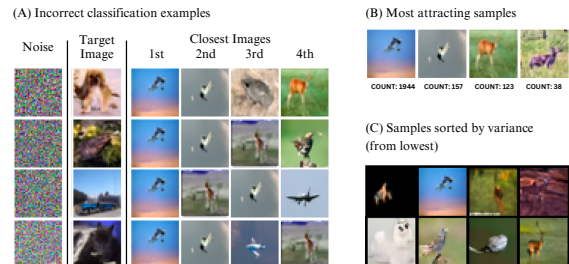


Figure 13. Examples of incorrect assignments of initial noises to resulting images (A), two most noise-attracting images (B), and samples sorted in ascending order by variance of pixels for ADM-32 model trained on the **CIFAR-10** dataset.

T	ADM-32		ADM-64		ADM-256		LDM		DiT	
	$\mathbf{x}_0 \rightarrow \mathbf{x}_T$	$\mathbf{x}_T \rightarrow \mathbf{x}_0$								
10	90.3 $\pm$ 6.3	94.0 $\pm$ 2.6	99.4 $\pm$ 0.0	100 $\pm$ 0.0	100 $\pm$ 0.0	39.2 $\pm$ 6.2	100 $\pm$ 0.0	100 $\pm$ 0.0	100 $\pm$ 0.0	93.7 $\pm$ 7.2
100	98.9 $\pm$ 1.2	50.4 $\pm$ 1.9	100 $\pm$ 0.0	59.0 $\pm$ 7.1	100 $\pm$ 0.0	23.2 $\pm$ 4.8	100 $\pm$ 0.0	100 $\pm$ 0.0	100 $\pm$ 0.0	90.7 $\pm$ 10.1
1000	99.1 $\pm$ 1.0	46.8 $\pm$ 3.0	99.8 $\pm$ 0.2	44.6 $\pm$ 6.3	100 $\pm$ 0.0	25.0 $\pm$ 4.4	100 $\pm$ 0.0	100 $\pm$ 0.0	100 $\pm$ 0.0	96.7 $\pm$ 4.6
4000	99.1 $\pm$ 1.0	46.4 $\pm$ 3.0	99.5 $\pm$ 0.3	43.3 $\pm$ 6.7	-	-	-	-	-	-

(a) Assigning noise to the corresponding generated image ( $\mathbf{x}_0 \rightarrow \mathbf{x}_T$ ) and vice-versa ( $\mathbf{x}_T \rightarrow \mathbf{x}_0$ ).

T	ADM-32		ADM-64		ADM-256		LDM		DiT	
	$\mathbf{x}_0 \rightarrow \hat{\mathbf{x}}_T$	$\hat{\mathbf{x}}_T \rightarrow \mathbf{x}_0$								
10	66.4 $\pm$ 1.7	38.2 $\pm$ 5.1	64.4 $\pm$ 7.1	100.0 $\pm$ 0.0	0.7 $\pm$ 0.2	30.8 $\pm$ 4.3	100 $\pm$ 0.0	100 $\pm$ 0.0	99.8 $\pm$ 0.6	95.1 $\pm$ 6.4
100	16.4 $\pm$ 6.1	33.4 $\pm$ 2.7	8.6 $\pm$ 9.3	57.5 $\pm$ 7.3	4.1 $\pm$ 1.4	23.9 $\pm$ 5.0	100 $\pm$ 0.0	100 $\pm$ 0.0	99.5 $\pm$ 1.7	90.7 $\pm$ 10.3
1000	3.6 $\pm$ 2.2	40.9 $\pm$ 2.7	1.7 $\pm$ 1.3	44.7 $\pm$ 6.5	23.9 $\pm$ 5.2	25.4 $\pm$ 4.4	100 $\pm$ 0.0	100 $\pm$ 0.0	100.0 $\pm$ 0.2	96.6 $\pm$ 4.6
4000	2.8 $\pm$ 2.2	41.9 $\pm$ 3.0	1.9 $\pm$ 1.4	43.5 $\pm$ 6.5	-	-	-	-	-	-

(b) Assigning images to the resulting latent encodings ( $\hat{\mathbf{x}}_T \rightarrow \mathbf{x}_0$ ) and vice-versa ( $\mathbf{x}_0 \rightarrow \hat{\mathbf{x}}_T$ ).

Table 11. Accuracy of the  $l_2$ -distance based assignment technique for both image $\leftrightarrow$ noise (a) and image $\leftrightarrow$ latent (b) mappings across varying number of diffusion steps  $T$ . For pixel DMs, only the image-to-noise ( $\mathbf{x}_0 \rightarrow \mathbf{x}_T$ ) mapping is feasible. On the other hand, for the latent space models, we correctly predict assignments in all directions.

## F. Replacing diffusion model predictions during inversion

In Sec. 5 we investigate how Diffusion Model’s prediction approximation error in first inversion steps affect final latent encodings. Here, we present more results for those experiments.

### F.1. Impact of replacing diffusion model predictions during inversion on interpolation

In Tab. 12, we show, for DiT model, that replacing the model’s predictions in the first 3 (6%) inversion steps halves the difference between the quality of interpolations resulting from latents when compared with the noise ones. Additionally, we observe an increase in Recall metric value for middle interpolation generations, suggesting that starting the DDIM inversion from 6% of the image corruption process could significantly increase the usefulness of the latents for interpolation and improve generation diversity.

Inversion predictions replaced (%T)	SLERP $_{\lambda=0.5}$		
	FID $\downarrow$	Precision $\uparrow$	Recall $\uparrow$
$\emptyset$ (0%)	19.68	0.79	0.41
1 (2%)	19.70	0.80	0.41
1...3 (6%)	18.29	0.80	0.43
1...5 (10%)	17.51	0.81	0.43
1...10 (20%)	16.79	0.81	0.45
Noise (100%)	16.61	0.80	0.47

Table 12. Impact of DDIM Inversion approximation error in first noising steps on the quality of generations resulting from latent interpolations. For the DiT model, we observe that replacing noise approximations with ground truth one in the first 5 inversion steps leads to higher quality and diversity of interpolated images, as indicated by FID and Recall metrics.

### F.2. Impact of replacing diffusion model predictions during inversion on image editing

In Tab. 13, we provide metrics values for Fig. 7. Percentages in each row indicate what fraction of the first inversion steps have been replaced with ground truth DM outputs from the backward diffusion process. Values in Fig. 7 indicate the percentage of improvement in diversity or text alignment for generations in comparison to images sampled from pure latent obtained from standard DDIM Inversion.

Predictions replaced (%T)	Diversity against $I_S$				CLIP Alignment	
	DreamSim $\uparrow$	LPIPS $\uparrow$	SSIM $\downarrow$	DINO $\downarrow$	$P_S \downarrow$	$P_T \uparrow$
$\emptyset$ (0%)	0.68 $\pm$ 0.13	0.56 $\pm$ 0.13	0.26 $\pm$ 0.15	0.22	0.543	0.568
1 (2%)	0.68 $\pm$ 0.13	0.56 $\pm$ 0.13	0.26 $\pm$ 0.15	0.22	0.471	0.667
1...3 (6%)	0.68 $\pm$ 0.13	0.57 $\pm$ 0.13	0.26 $\pm$ 0.15	0.22	0.468	0.673
1...5 (10%)	0.69 $\pm$ 0.13	0.57 $\pm$ 0.13	0.26 $\pm$ 0.15	0.22	0.465	0.676
1...10 (20%)	0.69 $\pm$ 0.13	0.57 $\pm$ 0.13	0.25 $\pm$ 0.14	0.20	0.462	0.681
Noise (100%)	0.71 $\pm$ 0.12	0.59 $\pm$ 0.12	0.23 $\pm$ 0.13	0.17	0.456	0.689

(a) Diffusion Transformer

Predictions replaced (t)	Diversity against $I_S$				CLIP Alignment	
	DreamSim $\uparrow$	LPIPS $\uparrow$	SSIM $\downarrow$	DINO $\downarrow$	$P_S \downarrow$	$P_T \uparrow$
$\emptyset$ (0%)	0.61 $\pm$ 0.12	0.33 $\pm$ 0.11	0.41 $\pm$ 0.14	0.42	0.353	0.614
1 (2%)	0.61 $\pm$ 0.12	0.33 $\pm$ 0.11	0.40 $\pm$ 0.14	0.41	0.352	0.615
1...3 (6%)	0.64 $\pm$ 0.11	0.36 $\pm$ 0.11	0.38 $\pm$ 0.13	0.39	0.334	0.632
1...5 (10%)	0.64 $\pm$ 0.11	0.36 $\pm$ 0.11	0.37 $\pm$ 0.13	0.38	0.327	0.637
1...10 (20%)	0.65 $\pm$ 0.10	0.36 $\pm$ 0.11	0.37 $\pm$ 0.13	0.37	0.313	0.645
Noise (100%)	0.66 $\pm$ 0.10	0.38 $\pm$ 0.11	0.34 $\pm$ 0.14	0.34	0.273	0.649

(b) Deepfloyd IF

Table 13. Impact of first DDIM inversion errors on diversity and text-alignment of generations from resulting latent as an input. For IF model (b), replacing the first inversion steps and denoising leads to more diverse generations against the source images  $I_S$ . For DiT (a), we show that such replacing improves the alignment between generation and target prompts, which the generation process is conditioned by, as indicated by the larger CLIP-T value for  $P_T$  and the smaller one for  $P_S$ .

## G. On Noise-Image-Latent relations during diffusion training

To further explore the relationships that exist between noises, generations, and latents, we study how the relationships between them change with the training of the diffusion model. We train two diffusion models from scratch and follow the setup from Nichol and Dhariwal [33] for two unconditional ADMs for the ImageNet ( $64 \times 64$ ) and CIFAR-10 ( $32 \times 32$ ) datasets. The CIFAR-10 model is trained for 700K steps, while the ImageNet model – for 1.5M steps, both with a batch size of 128. Models employ a cosine scheduler with 4K diffusion steps.

### G.1. Spatial relations of noise and latents over training time

We conclude our latent localization experiments by showing that our observations are persistent across the diffusion model training process. We generate  $N = 2048$  images with the final model, using implicit sampling with  $T = 100$  steps, and invert them to the corresponding latents using checkpoints saved during the training.

In Fig. 14, we show that both the angle adjacent to the noise  $\angle \mathbf{x}_T$  and the distance between the latent and noise  $\|\hat{\mathbf{x}}_T - \mathbf{x}_T\|_2$  quickly converge to the point that remains unchanged through the rest of the training, indicating that the relation between noises, latents, and samples is defined at the very early stage of the training. Additionally, we observe that the noise reconstruction error in DDIM Inversion does not degrade with the training progress.

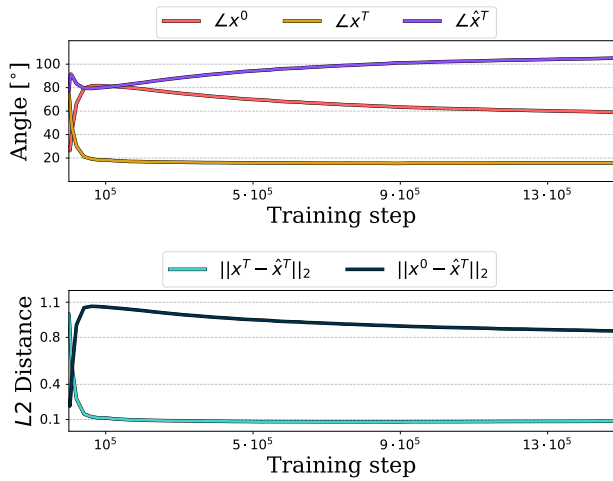


Figure 14. We investigate spatial relations between the noise  $\mathbf{x}_T$ , latents  $\hat{\mathbf{x}}_T$ , and generated images  $\mathbf{x}_0$  over training process of diffusion model. We show that those relations are defined at the early stage of the training.

### G.2. Image-to-noise distance mapping over training time

We analyze the image-noise mapping with  $l_2$ -distance from Sec. 4.3 over diffusion model training time. We sample  $N = 2000$  Gaussian noises and generate images from them using ADM models with  $T = 100$  diffusion steps, calculating the accuracy of assigning images to corresponding noises (and vice versa) using the smallest  $l_2$ -distance. In Fig. 15, we can observe, for both models, that the distance between noises and their corresponding generations accurately defines the assignment of initial noises given the generated samples ( $\mathbf{x}_0 \rightarrow \mathbf{x}_T$ ) from the beginning of the training till the end. At the same time, the accurate reverse assignment ( $\mathbf{x}_T \rightarrow \mathbf{x}_0$ ) can only be observed at the beginning of the training when the trained model is not yet capable of generating properly formed images. Already in the beginning phase of model training, the quality of noise to image mapping rapidly drops and does not change until the end of training.

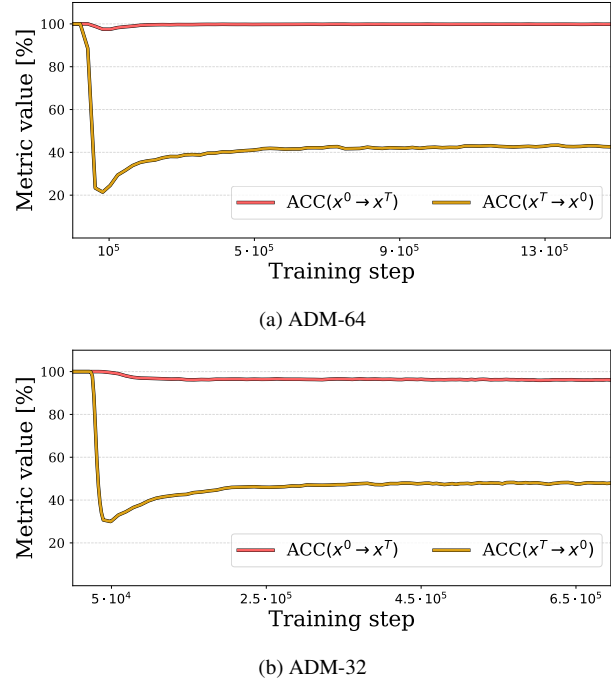


Figure 15. Accuracy of assigning initial noise given the generated sample ( $\mathbf{x}_0 \rightarrow \mathbf{x}_T$ ) and sample given the initial noise ( $\mathbf{x}_T \rightarrow \mathbf{x}_0$ ) when training the diffusion model. We can observe that from the very beginning of training, we can assign initial noise with a simple L2 distance while the accuracy of the reverse assignment rapidly drops.

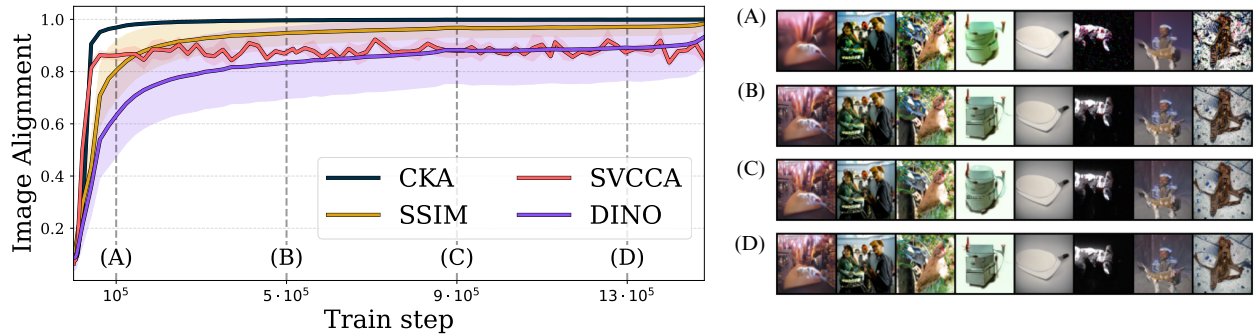


Figure 16. Similarity of the generations sampled from the same random noise at different stages of diffusion model’s training to the final outputs for ADM-64 model. Only after a few epochs does the model already learn the mapping between Gaussian noise and generations. Prolonged training improves the quality of samples, adding high-frequency features without changing their content. This can be observed through different image alignment metrics (left) and visual inspection (right).

### G.3. Image alignment over training time

Inspired by the noise-image mapping experiment, we investigate how the generations resulting from the same noise visually change over DM training time. Thus, for each training step  $n \in \{1 \dots 700K\}$  for CIFAR-10 and  $\{1 \dots 1.5M\}$  for ImageNet, we generate 2048 samples  $\{\mathbf{x}_{i,n}^0\}_{i=1}^{2048}$  from the same random noise  $\mathbf{x}_T^{\text{fixed}} \sim \mathcal{N}(0, \mathcal{I})$ , and compare them with generations obtained for the fully trained model. We present the visualization of this comparison in Fig. 16 using CKA, DINO, SSIM, and SVCCA as image-alignment metrics. We notice that image features rapidly converge to the level that persists until the end of the training. This means that prolonged learning does not significantly alter how the data is assigned to the Gaussian noise after the early stage of the training. It is especially visible when considering the SVCCA metric, which measures the average correlation of top-10 correlated data features between two sets of samples. We can observe that this quantity is high and stable through training, showing that generating the most important image concepts from a given noise will not be affected by a longer learning process. For visual comparison, we plot the generations sampled from the model trained with different numbers of training steps in Fig. 16 (right).

In Fig. 17, we visualize how the diffusion model learns the low-frequency features of the image already at the beginning of the fine-tuning when comparing generations from the next training steps against the generations after finished fine-tuning for the ADM-32 model trained on the CIFAR-10 dataset. In Fig. 18 (ADM-64) and Fig. 19 (ADM-32), we show additional examples illustrating how generations evolve over training for the same Gaussian noise  $\mathbf{x}_T$  using a DDIM sampler. Initially, low-frequency features emerge and remain relatively stable, while continued fine-tuning improves generation quality by refining only the high-frequency details.

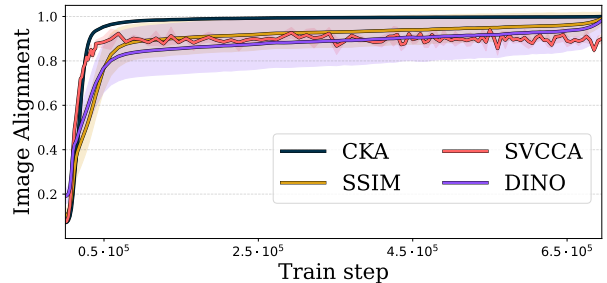


Figure 17. Similarity of the generations sampled from the same random noise at different stages of diffusion model’s training to the final outputs for ADM-32 (CIFAR-10). We plot CKA, SVCCA, SSIM, and DINO image alignment metrics and show that the diffusion model already learns the mapping between Gaussian noise and generations at the beginning of the training.



Figure 18. Examples of images sampled using DDIM scheduler from the same noise during the training process for the ADM-64 model trained on the ImageNet dataset.



Figure 19. Examples of images sampled using DDIM scheduler from the same noise during the training process for the ADM-32 model trained on the CIFAR-10 dataset.